

CrossMark
click for updatesCite this: *RSC Adv.*, 2014, 4, 59943

Stability of metal oxides against Li/Na carbonates in composite electrolytes

Francisco J. A. Loureiro, Surendran Rajesh, Filipe M. L. Figueiredo and Fernando M. B. Marques*

Solid oxide alkaline carbonate ($\text{Li}_2\text{CO}_3 : \text{Na}_2\text{CO}_3$, 1 : 1 molar ratio) composite electrolytes were prepared using different solid oxide matrices (TiO_2 , HfO_2 , Yb_2O_3 , Y_2O_3 , Dy_2O_3 , Gd_2O_3 and La_2O_3), to cover a wide range of ceramic chemical characteristics. The chemical and microstructural stability of these oxides with the mixed carbonates were studied by powder X-ray diffraction, scanning electron microscopy, infrared and laser Raman spectroscopic techniques after reacting them at 690 °C for 1 h in air. The electrical performance of selected composites was evaluated using impedance spectroscopy, in air. Amongst the oxides hereby tested, TiO_2 is found to be the most unstable in contact with the molten carbonates whereas Yb_2O_3 is quite stable. The corresponding composites have ionic conductivities ($3.3 \times 10^{-1} \text{ S cm}^{-1}$ at 580 °C, in air) close to those reported for state-of-the-art ceria-based composite electrolytes. A draft equivalent circuit model underlines the transport in the carbonate phase and across the carbonate/oxide interfaces as the dominant contributions to the total conductivity of these composites. $\text{Yb}_2\text{O}_3 + \text{Li}_2\text{CO}_3 : \text{Na}_2\text{CO}_3$ composites show chemical stability at operating temperatures in the order of 690 °C, standing as a potential candidate for intermediate temperature applications.

Received 29th September 2014
Accepted 5th November 2014

DOI: 10.1039/c4ra11446a

www.rsc.org/advances

Introduction

There is an ever-increasing demand for non-conventional energy conversion solutions, which are more efficient and environmentally friendly, in the context of an increasing concern about the lack of fossil fuels and their uncontrolled exploitation. Fuel cells are an alternative to the conventional systems of energy production owing to their vast diversity in output power, which ranges from a few watts to many megawatts. Among fuel cells, promising systems are the so-called intermediate temperature fuel cells usually designed for operating at 500–700 °C, essential conditions to tolerate the use of different fuels of moderate purity and to avoid catalysts based on noble metals.^{1–3}

The development of such devices is conditioned by many factors, namely the availability of electrolytes with high ionic conductivity (10^{-2} to $10^{-1} \text{ S cm}^{-1}$) and of electrodes with suitable stability and electrochemical performance.² Amongst promising electrolytes we find composites of a ceramic matrix based on rare earth-doped ceria (usually Gd or Sm) with a mix of molten alkali carbonates (normally of Li, Na and/or K).^{1,4,5} The existence of mixed ionic transport in these systems (*e.g.*, *via* oxide, carbonate ions and also alkali cations) attracts reasonable attention. The claimed evidence of protonic conductivity

seems established but still source of debate on its origin.^{6–8} The presence of different charge carriers in these composites makes them multifunctional materials with versatile applications including CO_2 separation membranes, steam electrolyzers, direct carbon fuel cells or the electrochemical synthesis of ammonia.^{9–13}

The influence of different microstructural and compositional effects on the performance of these composite electrolytes has been studied in detail in recent years.^{14–16} The chemical stability is a central problem in these composites, as molten alkali carbonates have a corrosive nature. For instance, a strong chemical interaction between the carbonates and Al_2O_3 and TZP (polycrystalline tetragonal zirconia, 3% mol of Y_2O_3) originated secondary compounds which deteriorated the electrical properties.¹⁶ The chemical inertness of Sm-doped or Gd-doped CeO_2 against the carbonates is one of the reasons (the high oxygen ionic conductivity being another) why the majority of the recently studied composite electrolytes involves ceria.^{16–18} Earlier work on Molten Carbonate Fuel Cells adopted LiAlO_2 as matrix, due to its high chemical stability in the highly corrosive carbonate medium.¹⁹ Few studies were also done involving proton conducting electrolytes like BCY (yttria-doped BaCeO_3) or BZY (yttria-doped BaZrO_3) as oxide matrix.^{8,20} Apart from that, less attention has been paid so far to develop alternative chemically stable oxide matrices against the molten carbonates.

In this work we have tried different ceramic oxides to evaluate their potential as matrix in composite electrolytes. In simple M_mO_n type systems, oxide-ion conductivity is only substantial in fluorite-

Department of Materials and Ceramic Engineering, CICECO, University of Aveiro, Aveiro 3810 193, Portugal. E mail: fmarques@ua.pt; Fax: +351234370204; Tel: +351234370269

type structures, mostly derivatives of ZrO_2 and CeO_2 , when suitably doped. Rare-earth sesquioxides have much lower levels of conductivity, but show protonic conductivity when appropriately doped with divalent cations.²¹ Merging of representatives of both families of oxides provides a wide range of acidic–basic characteristics to be tested with respect to stability when in contact with the molten carbonates. The selected oxides were Y_2O_3 and La_2O_3 (basic), Gd_2O_3 , Dy_2O_3 , Yb_2O_3 and Gd-doped CeO_2 (amphoteric), HfO_2 and TiO_2 (acid), listed in order of increasing acidity.²² The cations of acidic oxides belong to the group IV of the Periodic Table, while the remaining are lanthanides, and Y_2O_3 because of its chemical affinity with this group. Mixed oxides involving more than one cation sublattice (e.g., perovskites derived from LaGaO_3) also possess high ionic conductivity, but remained outside the scope of the present study.

As a summary, this work comprises a study of the stability of several oxides in contact with molten carbonates at temperatures close to 700 °C, aiming at the identification of potential trends for the development of alternative matrices. The total conductivity of the most stable composites is assessed as a complement.

Experimental

The composites starting materials were Y_2O_3 , La_2O_3 , Gd_2O_3 , Dy_2O_3 , Yb_2O_3 , HfO_2 , TiO_2 , Li_2CO_3 and Na_2CO_3 (Sigma Aldrich) and $\text{Ce}_{0.9}\text{Gd}_{0.1}\text{O}_{2-\delta}$ (CGO, from Praxair), all of them having >99.9% purity. CGO was here used as a reference material, for being well studied and known as a stable oxide matrix. The carbonate mixture used in this study (1 : 1 molar ratio) is close to the eutectic composition of Na_2CO_3 : Li_2CO_3 (0.48 : 0.52) and will be hereby referred to as LNC. Composites were prepared by mixing the precursors in a high-energy planetary ball mill (Retch PM200) using Nylon jars and zirconia balls (with 3 mol% of Y_2O_3), at 650 rpm for 30 min. The level of zirconia contamination resulting from high-energy milling in similar conditions is typically lower than 0.25 mass%.²³ XRD and SEM/EDS analyses confirmed no sign of significant contamination. The obtained powders were shaped into pellets of 10 mm diameter by uniaxial pressing at 200 MPa, and heat-treated at 690 °C for 1 h in air.

The sintered samples were crushed and the chemical stability of the oxides with the carbonates was studied through powder X-ray diffraction (XRD, Rigaku Geigerflex D/Max-C Series), infrared spectroscopy (FTIR-ATR, Bruker Tensor27) and laser Raman spectroscopy (Bruker RFS/100S, wavelength: 1064 nm). Another set of samples was also sintered under the same conditions and studied by electrochemical impedance spectroscopy using one LCR meter (Agilent 4210 A), in the temperature range of 300–580 °C, after applying Au electrodes. The microstructure of the samples was studied by scanning electron microscopy (SEM, Hitachi SU-70).

Results and discussion

Stability and structural analysis

The present information on the chemical stability of oxides against the LNC molten carbonates provides a fast screening of

potential candidate materials. It should be noticed that previous work on the reactivity of rare-earth oxides with Li_2CO_3 (ref. 24) can only be used for qualitative comparison purposes. With a melting point of 723 °C, the interaction of Li_2CO_3 with these oxides at temperatures below 700 °C is certainly distinct from what we might expect in the presence of LNC, melting at about 500 °C (eutectic temperature). In fact, interfaces between liquid and solid are expected to be larger than between the corresponding solids, and the rates for interfacial reactions and mass transport mechanisms are enhanced.

All XRD patterns obtained for the composites are shown in Fig. 1, with the peak intensities normalized against the major peak height in each pattern. As such, in the presence of only low intensity peaks the background line appears irregular and enhanced with respect to those patterns where one peak is clearly dominant. This situation is observed specially in the cases of composites including TiO_2 , HfO_2 , and Gd_2O_3 . This will be further related with the presumption of significant reactivity with vanishing of the major peaks from the precursor oxide.

With CGO + LNC, our reference system, we see the major oxide peaks with very weak traces of crystalline carbonates since these become amorphous after melting and furnace cooling, in agreement with previous reports.^{15,16} Likewise, several composites involving sesquioxides (Yb_2O_3 + LNC and Dy_2O_3 + LNC and also Y_2O_3 + LNC) show similar XRD patterns, dominated by the high intensity oxide peaks (Fig. 1). In the case of

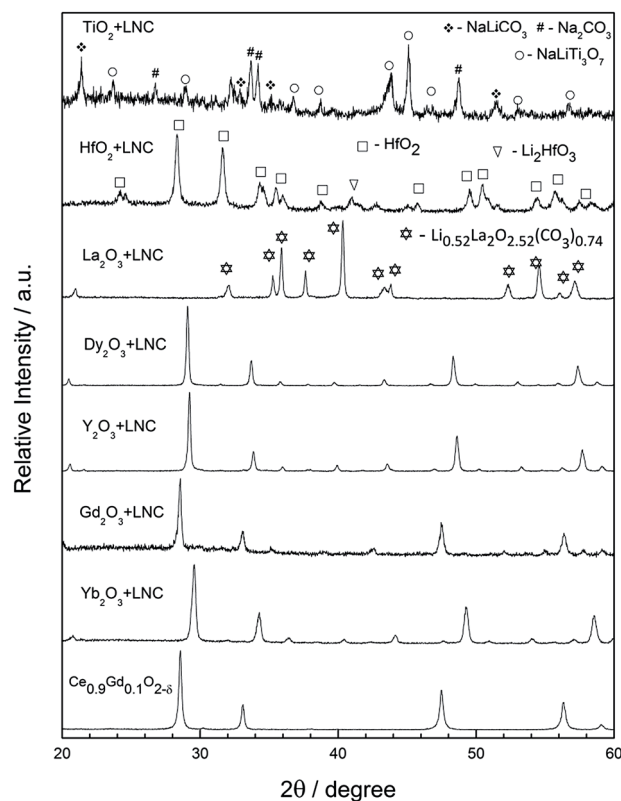


Fig. 1 XRD pattern of oxide/carbonate composites after heat treatment at 690 °C for 1 h. Each pattern is normalized to the most intense peak, thus appearing with the same relative intensity scale.

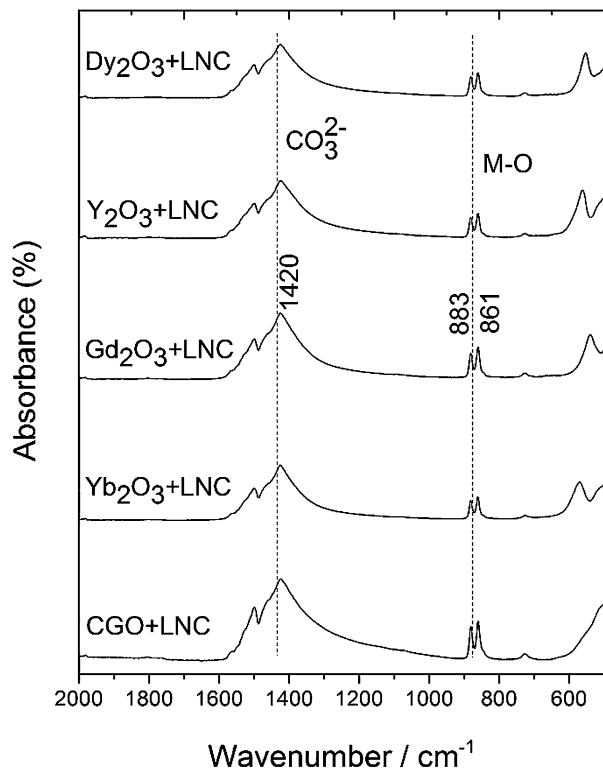


Fig. 2 FTIR-ATR spectra of composites after sintering.

Yb₂O₃, the most interesting result as detailed later, the positions of the XRD peaks before and after joint firing were preserved within the precision of the adopted measuring conditions, suggesting that the solubility of Li⁺ or Na⁺ is rather limited, if any, in this case.

The Gd₂O₃ reflections in the corresponding composite XRD pattern are clearly less intense than for the other rare earth oxides (noticed as much lower signal : background intensity ratio). It is already reported that the heat treatment of Gd₂O₃ under synthetic air (low concentration of CO₂) and in the presence of Li₂CO₃ leads to the formation of LiGdO₂ as secondary phase.²⁴ However, this reaction product was not observed here for Gd₂O₃ + LNC composites. La₂O₃ showed extensive reaction with LNC to form Li_{0.52}La₂O_{2.52}(CO₃)_{0.74} (ICDD file no. 01-084-1965). This phase has already been reported in the literature, due to reaction between La₂O₃ with Li₂CO₃, occurring under low CO₂ partial pressure.²⁴

HfO₂ + LNC results in a mixed phase of HfO₂ and Li₂HfO₃ (ICDD file no. 00-016-0898) even though the reaction is apparently not as significant as in the case of TiO₂, the latter leading to the formation of NaLiTi₃O₇ (ICDD file no. 00-052-0690). Further analyses of the allegedly more stable composite samples (those based on, CGO, Yb₂O₃, Gd₂O₃, Y₂O₃ and Dy₂O₃) using FTIR-ATR and laser Raman spectroscopies were carried out in order to assess the possible presence of species outside the detection limits of XRD.

The infrared spectra of all composite samples shown in Fig. 2 exhibit the same peaks, providing no additional information on any newly formed species. The wave number region

between 3500–2400 cm⁻¹, usually corresponding to hydrogenated species, is clean and hence avoided from the figure. Between 1600 and 800 cm⁻¹ we find the carbonate characteristic groups while typical metal-oxide vibrations are below 800 cm⁻¹. The broad bands observed near 1500 and 1420 cm⁻¹ correspond to stretching and the bands between 880 and around 860 cm⁻¹ to bending vibrations of O–C–O bonds of CO₃²⁻ ions.^{25,26}

The laser Raman spectra of the sintered composite samples are shown in Fig. 3. The vibrations corresponding to symmetric stretching of CO₃²⁻ are observed around 1072 cm⁻¹ and as a weak band at around 1090 cm⁻¹, with varying intensity for different composites.^{25–27} The vibrations of CO₃²⁻ are obscured by the high intensity of the oxide peaks. The bands corresponding to F_{2g} vibrations of rare earth oxides appear between 500–300 cm⁻¹. The peaks slightly change in their positions depending on the symmetry associated with rare earth oxides. As a tendency, we can see a decrease in the wave number with increasing atomic mass of the elements (in the case of Y and Gd).^{28,29} In Yb₂O₃ + LNC, no band is visible for either of the constituent phases, which is probably related to the wavelength used for the measurement (1064 cm⁻¹, infrared region). Yb₂O₃ emits very strongly in this region, possibly originating a luminescence phenomenon overlapping the Raman signal.^{28,29} The intensity of vibrations is very weak in the case of Gd₂O₃ + LNC, Dy₂O₃ + LNC, and Y₂O₃ + LNC samples and ended up with huge

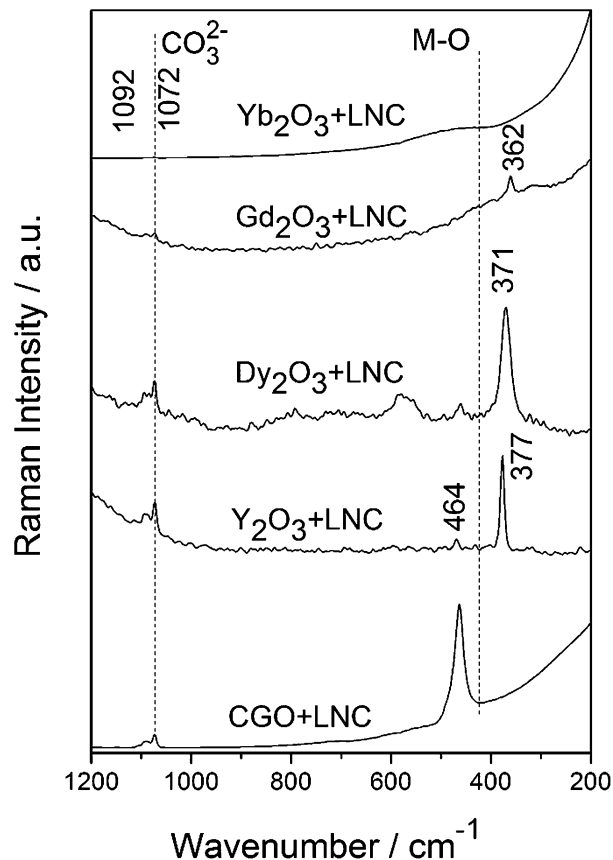


Fig. 3 Laser Raman spectra of composites after sintering.

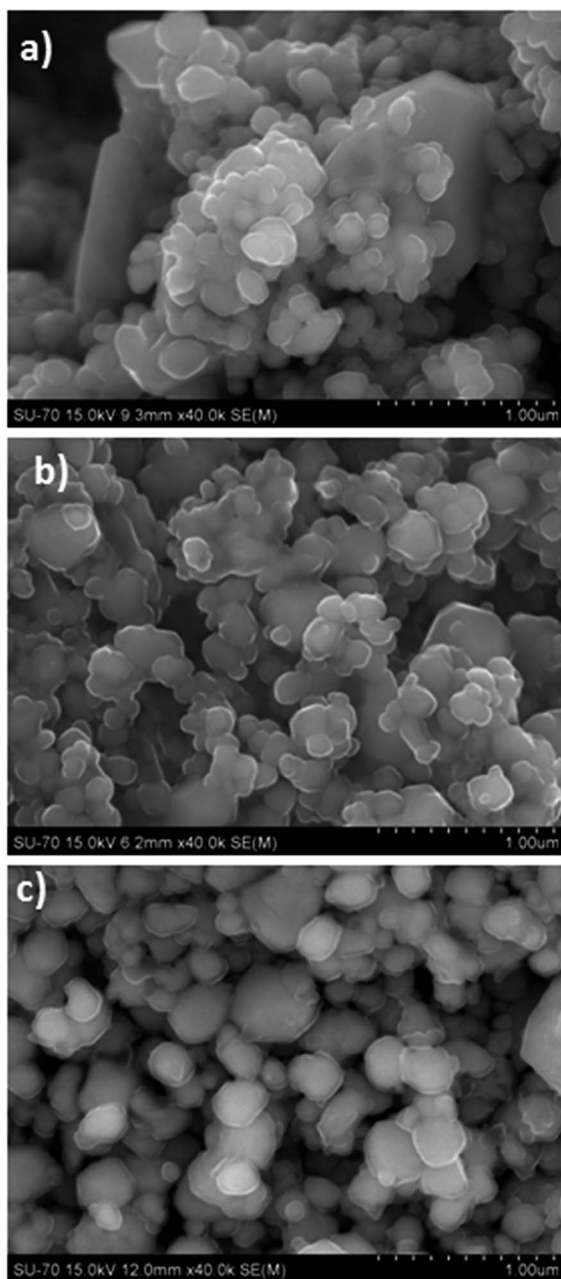


Fig. 4 Cross sectional SEM images of (a) $\text{Gd}_2\text{O}_3 + \text{LNC}$, (b) $\text{Y}_2\text{O}_3 + \text{LNC}$ and (c) $\text{Dy}_2\text{O}_3 + \text{LNC}$ composites after sintering.

noise in the base line. However, there are no extra peaks corresponding to new phases formed after reaction with the alkali carbonates.

Microstructural analysis

The evaluation of the microstructure, mainly the dispersion of both phases (oxide and carbonate), and the existence of porosity was evaluated by SEM. Representative pictures are shown in Fig. 4, taken from the fractured cross section of the sintered electrolytes.

Fig. 4a–c are SEM images of the $\text{Gd}_2\text{O}_3 + \text{LNC}$, $\text{Y}_2\text{O}_3 + \text{LNC}$ and $\text{Dy}_2\text{O}_3 + \text{LNC}$ samples, respectively. These observations

confirm the presence of large open porosity, unusual in the case of CGO + LNC composites with similar volume fractions of oxide and salt (see Fig. 5b, introduced later). These changes, detected by simple inspection of these samples by SEM, suggest that some chemical interaction with gas release occurred in these composites. According to reaction 1, involving one generic rare earth oxide (R_2O_3) and Li_2CO_3 as example of alkaline carbonate, formation of CO_2 is expected from the decomposition of the carbonates when reacting with the sesquioxides:²⁴



If this reaction occurs in the presence of molten carbonates, we might expect the formation of bubbles within the sample due to local built-in gas pressure. Molten carbonates are also expected to be dragged, accumulating in localized areas to keep open access to the expelled gas. These comments match closely the observed microstructural characteristics of these samples, where some regions were clearly flooded with the carbonates. It is, however, important to note that even within the highly porous regions there is a thin film covering the oxide particles.

For samples $\text{Yb}_2\text{O}_3 + \text{LNC}$ (Fig. 5a) and $\text{CGO} + \text{LNC}$ (Fig. 5b), we can observe the typical microstructures of almost fully dense composite electrolytes with oxide grains (light grey) dispersed within the (darker) carbonate phase. Oxide particles with

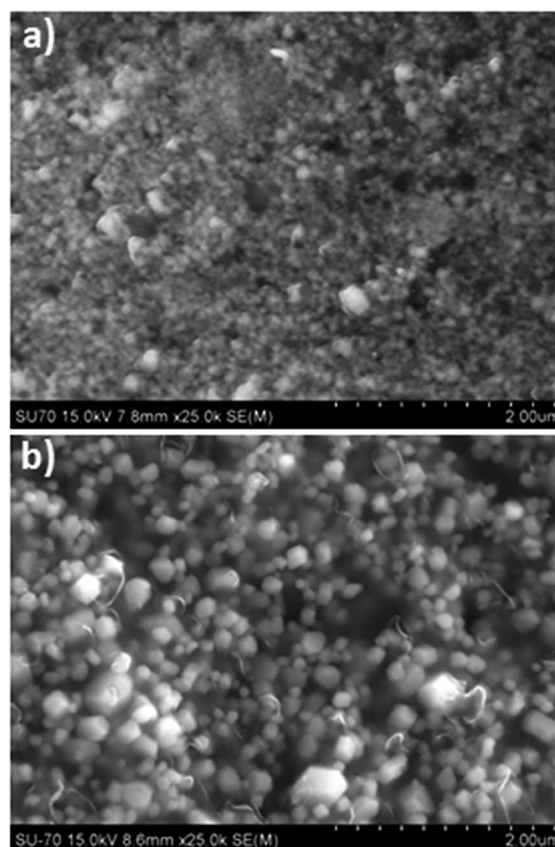


Fig. 5 Cross sectional SEM images of (a) $\text{Yb}_2\text{O}_3 + \text{LNC}$ and (b) $\text{CGO} + \text{LNC}$ composites after sintering.

distinct degrees of agglomeration/bonding are observed, but only in certain regions. The low particle agglomeration results in modest interconnectivity of the ceramic phase certainly related to the low sintering temperature (690 °C), far below the normal sintering temperature of these oxides. The light sintering of the ceramic phase is aided by the liquid phase that forms upon the fusion of the carbonates, although there is neither significant grain growth nor a high degree of oxide percolation. Combined SEM/EDS analysis of these fired mixtures was unable to detect any unusual microstructural feature or compositional difference within the spatial resolution of these techniques.

Summarizing the major microstructural characteristics found with both sets of composites, in Fig. 4a–c we could identify locally the apparent predominance of the oxide phase, suggesting significant decomposition or migration of the carbonates from specific composite areas. On the contrary, in Fig. 5a and b, the relative proportion of both phases seems better balanced, as expected from their nominal compositions.

Since in several cases the structural and microstructural characterization just presented provided mostly clues on possible interaction between the composite phases, in order to obtain further experimental evidence an additional approach was used in the characterization of these composites. Selected sintered samples were subjected to a cycle of annealing treatments in different atmospheres, following the $\text{CO}_2 \rightarrow \text{O}_2 \rightarrow \text{H}_2$ sequence. These samples were weighed after exposure to each atmosphere. Note that the initial mass of the composite was only considered after sintering in air to prevent the impact of the presence/loss of organic compounds (due to grinding in a Nylon container) and humidity potentially absorbed while stored after shaping. Of course, this procedure also excludes the assessment of any weight loss during sintering determined by early decomposition or reactivity between phases, but the relevance of this fact will appear as secondary after the results reported below. This study was conducted with CGO + LNC, Yb_2O_3 + LNC and Gd_2O_3 + LNC composites, and the results are

presented in Fig. 6. The first two composites were selected for being representative of the best stability (XRD and SEM) while the latter composite was selected for being representative of those composites (Gd_2O_3 + LNC, Y_2O_3 + LNC and Dy_2O_3 + LNC) showing what might be described as intermediate reactivity level.

As shown in Fig. 6, an increase in mass, sharp in case Gd_2O_3 + LNC and less perceptible in the composites CGO + LNC and Yb_2O_3 + LNC, is observed after exposure to CO_2 . This mass gain decreased immediately afterwards on moving to oxygen and furthermore until the end of the gas annealing sequence in hydrogen. The early mass gain confirms the recovery of carbonates after reaction or partial decomposition during sintering, probably corresponding to reaction (1) in the reverse direction, or to any other complementary/additional reversible process involving CO_2 . In fact, Scaccia *et al.*³⁰ used Gd_2O_3 as additive to the molten eutectic mixture of Li_2CO_3 and Na_2CO_3 and observed that Gd_2O_3 reacts with CO_2 forming $\text{Gd}_2\text{O}_2\text{CO}_3$. Even though we do not have any direct evidence in the present study for the formation of $\text{Gd}_2\text{O}_2\text{CO}_3$, the increase in the weight could lead to the same conclusion. The above results confirm that CGO + LNC and Yb_2O_3 + LNC composites are the most stable in this range of demanding conditions. The feeble mass changes observed in these cases can be explained by the well-known tendency for slow decomposition of the molten alkaline carbonates in the absence of CO_2 .

A simple explanation for the reactivity of different oxides with the molten carbonates is difficult. One way to categorize these materials is based on their acid–base nature, using the so-called Smith coefficient. Accordingly, Y_2O_3 and La_2O_3 are basic while HfO_2 and TiO_2 are acid.²² Among the basic systems, La_2O_3 shows very high reactivity with the carbonates whereas Y_2O_3 (more basic) seems more stable, closer to the performance of oxides like Gd_2O_3 or Dy_2O_3 , positioned in the amphoteric/basic transition. For the opposite characteristics, the more acidic TiO_2 reacts more than HfO_2 under the same conditions.

Yamauchi *et al.*²⁴ studied the stability of a mixture of Li_2CO_3 with rare earth oxides and Y_2O_3 , in both air and CO_2 atmospheres, at different temperatures. They reported that the formation of oxycarbonate from the oxide is easier for the light than for the heavy rare earth oxides due to shortening of the RE– O^{2-} distance for a coordination number $\text{CN}(\text{RE}) = 5$. But this proposition fails to explain the stability of CeO_2 , a light rare earth oxide. On the other hand, the heavy rare earth oxides attempted in our studies (Dy_2O_3 and Yb_2O_3) show more stability, especially Yb_2O_3 . Furthermore, this type of analysis is obviously centered in one single type of possible products of reaction, thus unable to cover all possible reaction schemes.

While there seems to be no clear rationale or absolute tendency based on these results and criteria, interestingly, only the most amphoteric oxides among those now tested, such as Yb_2O_3 and CGO, seem stable when compared with the basic and acidic oxides. This idea can be further tested for further exploitation of new oxides either as matrix or as electrode materials.

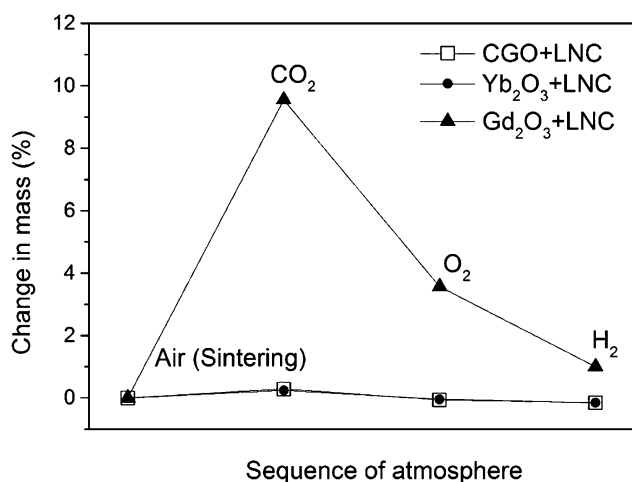


Fig. 6 Variation in mass of the CGO + LNC, Yb_2O_3 + LNC and Gd_2O_3 + LNC composites after annealing under variable atmosphere.

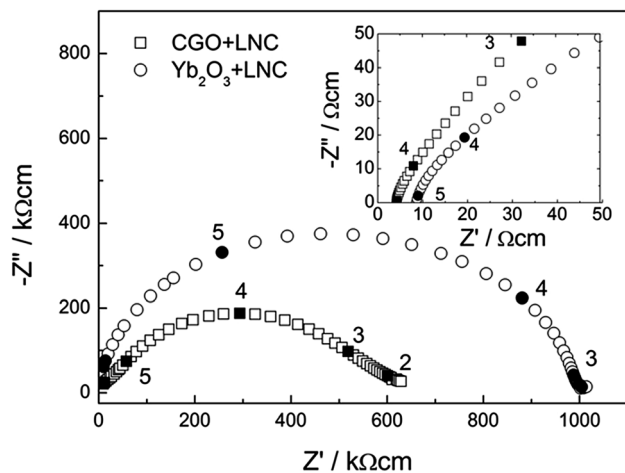


Fig. 7 Nyquist behavior of $\text{Yb}_2\text{O}_3 + \text{LNC}$ and $\text{CGO} + \text{LNC}$ composites at $300\text{ }^\circ\text{C}$ and at $580\text{ }^\circ\text{C}$ (inset), in air.

Impedance analysis

Among the ceramic oxides tested for their chemical stability with the molten carbonates, $\text{Yb}_2\text{O}_3 + \text{LNC}$ and $\text{CGO} + \text{LNC}$ were found to be the most stable composites by X-ray diffraction, vibrational spectroscopy, SEM and gravimetry under different atmospheres. $\text{CGO} + \text{LNC}$ is well studied providing the reference for performance of newly tested materials. Hence, it is reasonable to compare the electrochemical performances of $\text{Yb}_2\text{O}_3 + \text{LNC}$ composites with that of the $\text{CGO} + \text{LNC}$ composites. In order to have a broader understanding about the behavior of composites with different oxides, the electrical behavior of Gd_2O_3 and HfO_2 was also characterized. In this manner the selected range of composites includes examples of high reactivity, modest reactivity and no reactivity.

Fig. 7 shows the impedance behavior of $\text{Yb}_2\text{O}_3 + \text{LNC}$ and $\text{CGO} + \text{LNC}$ composites at $300\text{ }^\circ\text{C}$, which is lower than the melting temperature of carbonates. The impedance at $300\text{ }^\circ\text{C}$ is important, even though this temperature is much lower than the normal working conditions, since the spectra contain information that can be correlated with the composite composition and microstructure.¹⁸ The significantly depressed impedance arc observed in the case of $\text{CGO} + \text{LNC}$, with vestiges of a small arc at high frequency, suggests the superposition of the usual contributions of the ceramic phase (CGO bulk and grain boundary), somewhat faded by the poor connectivity between ceramic grains, and the additional impact of the electrical pathway *via* carbonates.¹⁸

A single amorphous phase would normally cause only the presence of one single arc with light depression, as found for LNC alone.³¹ An extensive analysis on capacitive and resistive contributions from the oxide and carbonate phase in CGO and CeO_2 -based composites using adequate equivalent circuits was recently presented.³² Following this intuitive analysis, the depressed arc obtained in $\text{CGO} + \text{LNC}$ composites can be fitted to an equivalent circuit consisting of a branch that includes a series association of two $\text{R}||\text{CPE}$ elements (accounting for CGO bulk and interfacial impedances) in parallel with another branch comprising just one $\text{R}||\text{CPE}$ circuit, corresponding to the mixed carbonates. According to this notation R represents a resistor, CPE a constant phase element and $||$ is a symbol representing the parallel association of these two circuit elements.

In the case of $\text{Yb}_2\text{O}_3 + \text{LNC}$ composites, the somewhat depressed semicircle and the sharp increase of the phase angle towards the two extremes of the frequency range suggest also more than one contribution in series, with distinct relaxation frequencies. This result is somewhat unexpected in view of the electrical characteristics of pure Yb_2O_3 where we might expect dominant but modest electronic conductivity. Indeed, in the alike case of pure ceria, no obvious separation of bulk and grain boundary contributions was noticed.^{32, 34} In such conditions the impedance spectra of composites should consist mostly of one regular arc, closer to a perfect semicircle, as previously discussed.

At high temperature only the resistive component of the composite electrolytes is observed, which corresponds to the value of Z' at the high frequency intersection of the visible electrode arc with the real axis (Fig. 7 inset). The resistivity of the electrolyte decreases dramatically at high temperature, passing from $600\text{--}630\text{ k}\Omega\text{ cm}$ at $300\text{ }^\circ\text{C}$ to $3\text{--}6\text{ }\Omega\text{ cm}$ at $580\text{ }^\circ\text{C}$ due to melting of carbonates around $500\text{ }^\circ\text{C}$.

A more detailed analysis of the conductivity of the composites and the individual components is useful at this point of discussion. Table 1 shows the conductivity of sintered Gd_2O_3 , Yb_2O_3 , HfO_2 and CGO single phase ceramics and also of their composites when mixed with LNC , either from own results or from the literature. The conductivity of $\text{CGO} + \text{LNC}$ composites is between the conductivity of the individual components, and it is the only case where we may clearly find the usual blending of properties due to mixture of constituents. On the other hand, $\text{Gd}_2\text{O}_3 + \text{LNC}$ and $\text{Yb}_2\text{O}_3 + \text{LNC}$ composites apparently show slightly better conductivity than the constituent phases. However, distinct sources of data, materials (unknown purity and microstructures), and techniques employed (*e.g.*, dc *versus* ac in the case of oxides and composites, respectively) should be

Table 1 Conductivity of different oxides, mixed carbonates and composites at $300\text{ }^\circ\text{C}$ in air

σ at $300\text{ }^\circ\text{C}$ (S cm^{-1})	LiNaCO_3	CGO	Yb_2O_3	Gd_2O_3	HfO_2
Single phase carbonates or oxides	4.0×10^{-7a}	7.7×10^{-5a}	5.3×10^{-8b}	5×10^{-9b}	4.9×10^{-9b}
Composites (50 : 50 vol%)		6.7×10^{-6}	8.4×10^{-7}	4.8×10^{-7}	1.4×10^{-7}

^a Own data from.³² ^b Data from,^{33,34} dc measurements.

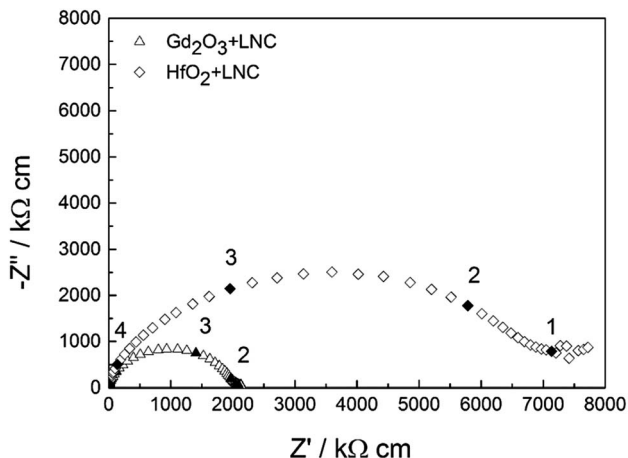


Fig. 8 Nyquist behavior of $\text{Gd}_2\text{O}_3 + \text{LNC}$ and $\text{HfO}_2 + \text{LNC}$ composites at $300\text{ }^\circ\text{C}$, in air.

considered before any attempt to speculate on these small differences. In fact, in all these cases the conductivity of the composite is of the order of magnitude of the single carbonate phase. The explanation for the poor conduction in the $\text{HfO}_2 + \text{LNC}$ must rely on the reactivity of HfO_2 with Li to form Li_2HfO_3 , which is clear from the X-ray diffraction analysis.

While data just discussed on total conductivity provides little insight on the electrical microstructure of composite materials, the low temperature impedance plots of $\text{CGO} + \text{LNC}$ and $\text{Yb}_2\text{O}_3 + \text{LNC}$ (Fig. 7), including depressed semicircles, indicate the presence of multiple contribution towards the total conductivity. In turn, the spectrum for $\text{HfO}_2 + \text{LNC}$ shows a regular semicircle (Fig. 8), indicating a more homogeneous electrical microstructure, even if consisting of distinct phases with distinct characteristics. This suggests a dominant and contiguous electrical pathway. For $\text{Gd}_2\text{O}_3 + \text{LNC}$ (Fig. 8) the situation is somewhat similar to the most stable composites. However, given the higher conductivity and stability of $\text{Yb}_2\text{O}_3 + \text{LNC}$ composites within the newly tested materials, the following discussion will be centered in these materials.

In a generalized point of view, the impedance of $\text{Yb}_2\text{O}_3 + \text{LNC}$ composites can be originated mainly from 4 parallel contributions as depicted by the model schematized in Fig. 9. Branch I represents the contribution from the oxide phase, which, considering the very low conductivity of Yb_2O_3 (one order of magnitude less than for pure LNC), may be considered as a secondary contribution to the total conductivity of the composite. As such, the dominant ionic transport through the contiguous carbonate phase (branch IV) is more likely considering the slightly higher conductivity of this phase in comparison with pure Yb_2O_3 . An enhanced concentration of defects at the oxide/carbonate interface due to a space charge effect or the solubility of small amounts of Li^+ and/or Na^+ at the surface of the Yb_2O_3 particles (in all aspects similar to that invoked to explain the composite effect on CeO_2/LNC mixtures³¹) may represent a third region with higher conductivity than the bulk carbonate, which would correspond to another parallel path (branch III). The hypothesis of having this third path

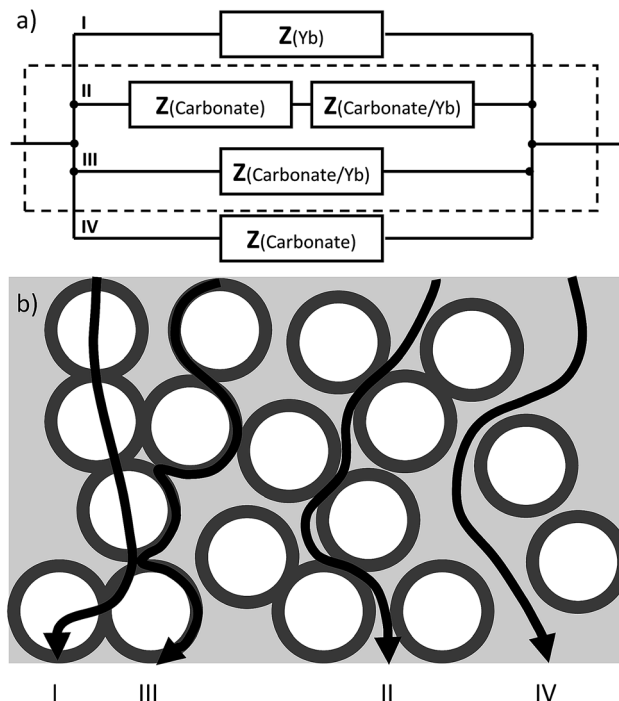


Fig. 9 (a) General equivalent circuit model grouping all the schematic situations described in (b), with different contributions to the total impedance of $\text{Yb}_2\text{O}_3 + \text{LNC}$ composites, namely from the bulk of each phase and from the interfaces between them.

representing a major contribution to the total charge transport implies a higher conductivity of the composite in comparison to the pure carbonate, which is not the case according to Table 1 (and also in contradiction with compositional effects discussed ahead in this paper). Moreover, a parallel branch with similar resistive and capacitive characteristics cannot be used to deconvolute the two contributions with distinct relaxation frequencies apparent in the impedance spectrum of the $\text{Yb}_2\text{O}_3/\text{LNC}$ composite in Fig. 7. From the viewpoint of equivalent circuit modeling, the easiest approach is to consider at least two impedance contributions in series, which we may ascribe in the present case to transport within the carbonate bulk and across the carbonate/ Yb_2O_3 interfacial regions (branch II in Fig. 9). The similarities between the schematized branch II in Fig. 9 and the microstructure of the real composite are obvious considering the homogeneous dispersion of the Yb_2O_3 particles within the carbonate matrix depicted in Fig. 5a.

Considering the above discussion, as an attempt to further elucidate on potential interfacial effects and likely transport mechanisms, the effect of the oxide content and the degree of homogeneity of particle dispersion on the electrical properties of the composites was studied by extending the compositional range to composites with 25 and 75 vol% of Yb_2O_3 . Furthermore, the composites were made both by high-energy milling or light hand milling, both followed by the same heat treatment in air at $690\text{ }^\circ\text{C}$. By comparing the microstructures of both series of samples (Fig. 10), it can be seen that the fine and homogeneous dispersion of the oxide particles in the composites prepared *via*

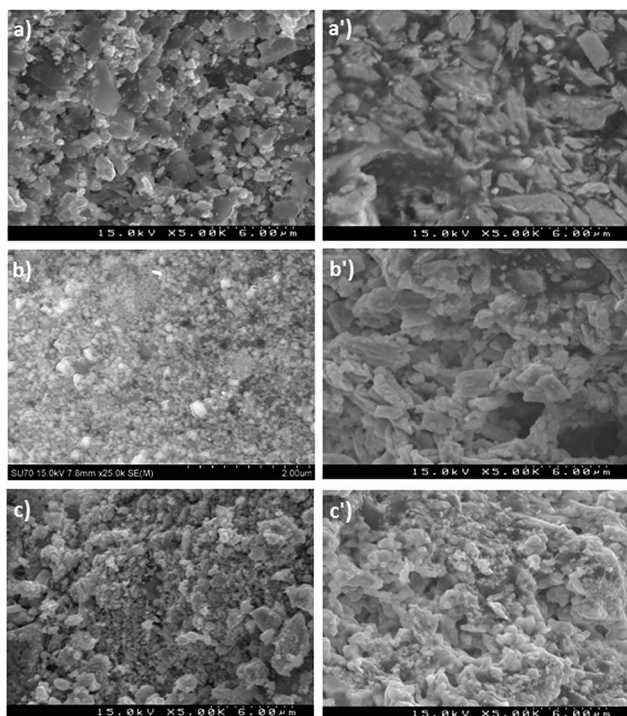


Fig. 10 (a–c) Microstructure of the high energy milled samples with 25, 50, 75 vol% of ytterbia, respectively; (a'–c') correspond to hand mixed samples.

high-energy milling is lost in the hand mixed materials, where the micron-sized oxide particles are mixed with large pieces of carbonate, producing a much smaller carbonate/ Yb_2O_3 interfacial area.

These microstructural differences are reflected in the obtained impedance spectra, with those for the hand-milled composites depicting a single, slightly depressed semicircle compatible with the dominating response of the pure carbonate phase (Fig. 11). In contrast, the shape of spectra of the composites prepared by high energy milling suggest the presence of a second contribution at lower frequency, which according to the model presented in Fig. 9 can be ascribed to the impedance of the carbonate/ Yb_2O_3 interfaces. In agreement with the model (Fig. 9, branch II), the spectra could be fitted with a series association of two simple parallel $\text{R}||\text{CPE}$ circuits.

The CPE impedance is defined as $Z_{\text{CPE}} = [Y_0(i\omega)^n]^{-1}$, where ω is the angular frequency and Y_0 and n are the usual parameters characterizing the pseudo-capacitance and the phase angle, respectively. The capacitance in the case of the $\text{R}||\text{CPE}$ circuit is given by $C = R^{1/n-1}Y_0^{1/n}$.

The fitting results are listed in Table 2 using the subscripts “carb” and “int” to identify the carbonate and the interface contributions, respectively. These data reveal the lowest $R_{\text{carb}}:R_{\text{int}}$ ratio (~ 0.9) for the composite with equal fraction of each phase, in agreement with the high concentration of interfaces expected for this composition. Likewise, the composite with the highest carbonate content has the highest ratio ($R_{\text{carb}}:R_{\text{int}} \approx 2.6$), which can be seen as an indication of the poorly percolating network of interfaces due to the low volume fraction of

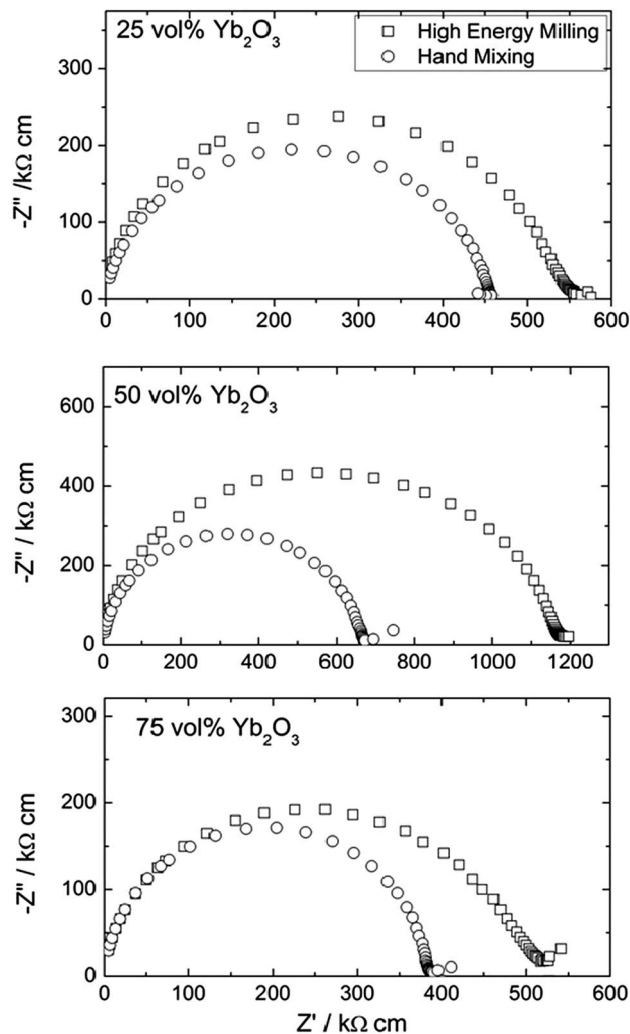


Fig. 11 Impedance behavior of the samples prepared through hand mixing and high energy milling with different volume fractions of Yb_2O_3 .

oxide particles. In contrast, $R_{\text{carb}}:R_{\text{int}} \approx 1.6$ characterizes an intermediate behavior for the composite with 75 vol% Yb_2O_3 , reflecting the higher fraction of oxide particles and their wetting by the carbonate phase.

While the shape of the spectra is coherent with the proposed model of transport in the carbonate phase and across the carbonate/oxide interfaces, the total resistance of the samples shows a non-monotonous variation with respect to the oxide loading. The samples with 50 vol% Yb_2O_3 have the highest resistance when compared with the other two volume fractions, thus suggesting a negative effect of the interface on the total conductivity of the composites. However, we must also emphasize that the microstructures tend to be distinct, with higher porosity in the presence of higher ceramic content. This means that emphasis on an overall modest compositional dependence, where microstructural features might prevail, seems more wised than on waving tendencies.

The dependence of the conductivity as a function of temperature depicts the usual sudden increase in conductivity

Table 2 Fitting parameters from impedance spectra (measured at 300 °C) of high energy milled samples with different Yb₂O₃ volume fractions. Error (%) are given inside brackets

Parameter	25 vol% Yb ₂ O ₃ + LNC	50 vol% Yb ₂ O ₃ + LNC	75 vol% Yb ₂ O ₃ + LNC
R_{carb} (Ω cm)	3.9×10^5 (13.5)	5.37×10^5 (5.95)	3.13×10^5 (30.41)
$Y_{0 \text{ carb}}$ (pS s)	5.98 (15.6)	9.72 (4.74)	24.03 (20.84)
n_{carb}	0.98 (2)	0.93 (0.63)	0.91 (3.54)
C_{carb} (pF)	7.9	24.1	72.2
f_{peak} (kHz)	317	77.4	44.2
R_{int} (Ω cm)	1.5×10^5 (35.5)	6.3×10^5 (5.20)	1.96×10^5 (49.62)
$Y_{0 \text{ int}}$ (pS s)	648 (80.6)	57.67 (5.33)	453.88 (43.24)
n_{int}	0.74 (3.9)	0.87 (0.74)	0.80 (4.67)
C_{int} (pF)	19 400	335	6100
f_{peak} (kHz)	0.34	4.73	0.83

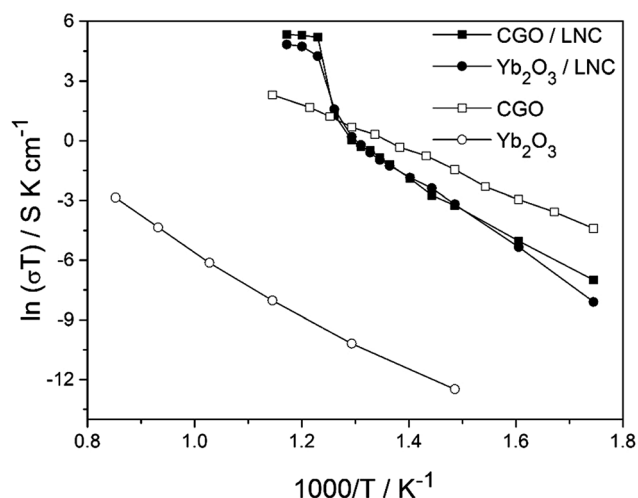


Fig. 12 Arrhenius behavior of CGO + LNC, Yb₂O₃ + LNC composites and CGO and Yb₂O₃ oxides (own data).

near the melting temperature of the carbonates (500 °C or 1000/ $T \approx 1.3 \text{ K}^{-1}$) (Fig. 12). Below and above this transition, the behavior follows a typical Arrhenius trend, with low activation energy ($\sim 50 \text{ kJ mol}^{-1}$) at high temperature, and higher values (between 120 and 130 kJ mol^{-1}) at low temperatures, in both cases close to the characteristic values of the molten and solid carbonates, respectively.^{35–37} The Arrhenius behavior of pure CGO and Yb₂O₃ sintered in air at 1550 and 1600 °C, respectively, are also included confirming that CGO is a well-known ionic conductor whereas Yb₂O₃ is a modest conductor.

Conclusions

Solid oxide–alkaline carbonate composite electrolytes were prepared using different ceramic matrices (TiO₂, HfO₂, Yb₂O₃, Y₂O₃, Dy₂O₃, Gd₂O₃ and La₂O₃) and Li₂CO₃ : Na₂CO₃ carbonate 1 : 1 molar mixtures. The chemical stability of these oxides against the mixed carbonates was studied using XRD, SEM, FTIR and Raman spectroscopies. TiO₂ is the most unstable among the studied oxides whereas Yb₂O₃ is quite stable in contact with the molten carbonates, apart from CGO here used as reference. The electrical performance of CGO + LNC and

Yb₂O₃ + LNC composites studied by impedance spectroscopy confirmed that Yb₂O₃ + LNC performs worst below the carbonates melting point but at higher temperature the conductivities almost match. A draft equivalent circuit model is suggested to explain the compositional and microstructural effects on the low temperature impedance of Yb₂O₃ + LNC composites, underlining the transport in the carbonate phase and across the carbonate/oxide interfaces as the dominant contributions to the total conductivity of these composites. Overall, Yb₂O₃ is a potential candidate for the development of intermediate temperature composite electrolytes considering the confirmed chemical stability and versatile potential to accommodate distinct types of defects when properly doped (oxide-ions and protons), typical feature of rare earth sesquioxides.

Acknowledgements

Financial support from FCT/COMPETE/FEDER (Portugal) through projects NANOMFC (New-INDIGO/0001/2013), CICECO - FCOMP-01-0124-FEDER-037271 (Ref. FCT PEst-C/CTM/LA0011/2013), and Investigador FCT 2013 ref. IF/01174/2013b is greatly appreciated. S. Rajesh thanks FCT for the post-doctoral grant (SFRH/BPD/76228/2011).

Notes and references

- 1 Y. Zhao, C. Xia, L. Jia, Z. Wang, H. Li, J. Yu and Y. Li, *Int. J. Hydrogen Energy*, 2013, **38**, 16498–16517.
- 2 D. J. L. Brett, A. Atkinson, N. P. Brandon and S. J. Skinner, *Chem. Soc. Rev.*, 2008, **37**, 1568–1578.
- 3 A. J. Jacobson, *Chem. Mater.*, 2010, **22**, 660–674.
- 4 M. Benamira, A. Ringuedé, L. Hildebrandt, C. Lagergren, R.-N. Vannier and M. Cassir, *Int. J. Hydrogen Energy*, 2012, **37**, 19371–19379.
- 5 B. Zhu, X. Liu, P. Zhou, Z. Yang, X. Yang and W. Zhu, *Electrochem. Commun.*, 2001, **3**, 566–571.
- 6 H. Nafe, *ECS J. Solid State Sci. Technol.*, 2013, **3**, N7–N14.
- 7 Y. Zhao, C. Xia, Y. Wang, Z. Xu and Y. Li, *Int. J. Hydrogen Energy*, 2012, **37**, 8556–8561.
- 8 T. Schober, *Electrochem. Solid-State Lett.*, 2005, **8**, A199–A200.

- 9 L. Fan, C. Wang, M. Chen and B. Zhu, *J. Power Sources*, 2013, **234**, 154–174.
- 10 L. Zhang, N. Xu, X. Li, S. Wang, K. Huang, W. H. Harris and W. K. S. Chiu, *Energy Environ. Sci.*, 2012, **5**, 8310.
- 11 B. Zhu, I. Albinsson, C. Andersson, K. Borsand, M. Nilsson and B.-E. Mellander, *Electrochem. Commun.*, 2006, **8**, 495–498.
- 12 L. Jia, Y. Tian, Q. Liu, C. Xia, J. Yu, Z. Wang, Y. Zhao and Y. Li, *J. Power Sources*, 2010, **195**, 5581–5586.
- 13 B. Zhu, X. Liu and T. Schober, *Electrochem. Commun.*, 2004, **6**, 378–383.
- 14 S. G. Patrício, C. M. C. Soares, C. F. N. Santos, F. M. L. Figueiredo and F. M. B. Marques, *Solid State Ionics*, 2014, **262**, 248–252.
- 15 A. S. V. Ferreira, C. M. C. Soares, F. M. H. L. R. Figueiredo and F. M. B. Marques, *Int. J. Hydrogen Energy*, 2011, **36**, 3704–3711.
- 16 A. Sofia, V. Ferreira, T. Saradha, F. L. Figueiredo and F. M. B. Marques, *Int. J. Energy Res.*, 2011, **35**, 1090.
- 17 X. Xu, W. Zhou and Z. Zhu, *RSC Adv.*, 2014, **4**, 2398.
- 18 C. M. C. Soares, S. G. Patrício, F. M. L. Figueiredo and F. M. B. Marques, *Int. J. Hydrogen Energy*, 2014, **39**, 5424–5432.
- 19 M. Mizuhata, A. Bienvenu Béléké, H. Watanabe, Y. Harada and S. Deki, *Electrochim. Acta*, 2007, **53**, 71–78.
- 20 K.-Y. Park, T.-H. Lee, J.-T. Kim, N. Lee, Y. Seo, S.-J. Song and J.-Y. Park, *J. Alloys Compd.*, 2014, **585**, 103–110.
- 21 Y. Larring and T. Norby, *Solid State Ionics*, 1995, **77**, 147–151.
- 22 D. W. Smith, *J. Chem. Educ.*, 1987, **64**, 480481.
- 23 P. Gonçalves and F. M. Figueiredo, *Solid State Ionics*, 2008, **179**, 991–994.
- 24 M. Yamauchi, Y. Itagaki, H. Aono and Y. Sadaoka, *J. Eur. Ceram. Soc.*, 2008, **28**, 27–34.
- 25 M. H. Brooker, *J. Chem. Phys.*, 1971, **54**, 4788.
- 26 W. R. Carper, P. G. Wahlbeck and T. R. Griffiths, *J. Phys. Chem. B*, 2012, **116**, 5559–5567.
- 27 J. B. Bates, M. H. Brooker, A. S. Quist and G. E. Boyd, *J. Phys. Chem.*, 1972, **76**, 1565–1571.
- 28 D. Chen, Y. Wang and M. Hong, *Nano Energy*, 2012, **1**, 73–90.
- 29 A. Ubaldini and M. M. Carnasciali, *J. Alloys Compd.*, 2008, **454**, 374–378.
- 30 S. Scaccia, S. Frangini and S. Dellepiane, *J. Mol. Liq.*, 2008, **138**, 107–112.
- 31 T. Saradha, A. S. Ferreira, S. G. Patrício, F. M. L. Figueiredo and F. M. B. Marques, *Int. J. Hydrogen Energy*, 2012, **37**, 7235–7241.
- 32 A. I. B. Rondão, S. G. Patrício, F. M. L. Figueiredo and F. M. B. Marques, *Electrochim. Acta*, 2013, **109**, 701–709.
- 33 G. V. S. Rao, S. Ramdas, P. N. Mehrotra and C. N. R. Rao, *J. Solid State Chem.*, 1970, **2**, 377–384.
- 34 A. Weyl and D. Janke, *J. Am. Ceram. Soc.*, 1996, **79**, 2145–2155.
- 35 T. Kojima, Y. Miyazaki, K. Nomura and K. Tanimoto, *J. Electrochem. Soc.*, 2007, **154**, F222–F230.
- 36 P. L. Spedding, *J. Electrochem. Soc.*, 1973, **120**, 1049–1052.
- 37 P. Cerisier and F. Roux, *J. Solid State Chem.*, 1977, **22**, 245–251.